Nanoscale

PAPER

View Article Online
View Journal | View Issue

Cite this: *Nanoscale*, 2023, **15**, 12558

Ultrasmall Pt NPs-modified flasklike colloidal motors with high mobility and enhanced ion tolerance†

Shurui Yuan,[a] Ling Yang,[b] Xiankun Lin *[a] and Qiang He *[a]

Received 6th June 2023,
Accepted 5th July 2023

DOI: 10.1039/d3nr02664g

rsc.li/nanoscale

Chemically powered colloidal motors propelled by the self-phoretic effect have attracted widespread attention. However, the low motion efficiency and ion tolerance hinder their application in complex media. Herein, we report a scalable and simple method to synthesize 2.6 nm Platinum nanoparticles (Pt NPs) in the nanoporous wall of carbonaceous flasklike colloidal motors in a ligand-free manner. The obtained Pt NPs-modified flasklike colloidal motors (Pt-FCMs) are propelled by the catalytic decomposition of H_2O_2 fuels. They exhibit ultrafast mobility with an instantaneous velocity of 134 μm s^{-1} at 5% H_2O_2, which is equivalent to 180 bodylengths per second. Particularly, these Pt-FCMs have an enhanced ion tolerance, due to the higher catalytic activity of small-sized Pt NPs in the carbonaceous wall. Furthermore, the direction of motion could be reversed by adding cationic surfactant cetyltrimethylammonium bromide. Such ultrasmall Pt NPs funtionalized flasklike colloidal motors exhibit a great potential utilization in the field of biomedicines and environmental technology.

Introduction

Chemically powered colloidal motors are capable of converting chemical energy into persistent swimming-like locomotion in fluids. Particularly, the colloidal motors propelled by the self-phoretic effect have garnered considerable attention since they can autonomously perceive the concentration gradient and exhibit chemotaxis and collective behaviours similar to that of living organisms.[1–6] Due to their remarkable performance, chemically powered colloidal motors are considered some of the most promising candidates for artificially intelligent colloid-scale machines,[7–9] and display great potential in the fields of biomedicines and environmental science.[10,11] However, the majority of chemically powered self-phoretic colloidal motors developed to date exhibit low velocity, especially if the colloidal motors have all the dimensions at the nanometer scale and have to overcome strong Brownian motion.[12] Moreover, the motion of these colloidal motors shows intolerance of high ionic strength in neutral ionic solutions, which means that these colloidal motors could not move in complex environments such as biological media.[13,14] The challenges greatly hinder the applications of the colloidal motors. Therefore, it is crucial to develop colloidal motors with high motion efficiency and enhanced ion tolerance.

Some strategies have been employed to improve the ion tolerance of colloidal motors, including coating a layer of polyelectrolytes,[15] optimizing the geometry to introduce structural nanopores,[16] and decreasing the characteristic size to nanometer scales.[17] In addition, some studies have reported that the ion quenching phenomena of the Pt-polystyrene Janus motors propelled by the catalytic decomposition of H_2O_2 only occur in the presence of neutral salt solutions such as NaCl, KBr, and so on. For an alkaline solution like NaOH, the quenching effect of ionic strength on the motion velocity is insignificant,[13,14] which may contribute to the alkaline environment facilitating the catalytic decomposition of H_2O_2 and compensating for the adverse effect of ionic strength on motor activity. Remarkably increasing the catalytic activity of colloidal motors may provide a simple but effective way to achieve enhanced ion tolerance and high motion velocity simultaneously without additional chemical modifications. The catalytic activity of nanoparticle catalyst is strongly dependent on the particle size and its distribution, with small and uniform nanoparticles typically resulting in high catalytic activity.[4,18] Traditional methods involve the addition of ligands to control the size and morphology of catalyst particles, resulting in small, uniform particles with high catalytic activity. However, the presence of ligands blocks the catalytic sites, resulting in the reduction of catalytic activity. The ligand-free

[a]*School of Medicine and Health, Harbin Institute of Technology, Yi Kuang Jie 2, Harbin 150080, China. E-mail: qianghe@hit.edu.cn, xiankunlin@hit.edu.cn*
[b]*Wenzhou Institute, University of Chinese Academy of Sciences, Wenzhou 325000, China*

† Electronic supplementary information (ESI) available. See DOI: https://doi.org/10.1039/d3nr02664g

synthesis can directly produce a nanocatalyst with the surface-clean property, which can lead to excellent catalytic activity. Therefore, using the ligand-free synthesis method to prepare small-size and uniform nanoparticle catalysts should be a reasonable way to prepare the highly active colloidal motors. The ligand-free ethylene glycol reduction method has been employed for the *in situ* growth of ultrasmall, uniformly sized platinum nanoparticles (Pt NPs) on carbon black[19] and multi-walled carbon nanotubes[20,21] with high catalytic activity.

Herein, we present the ethylene glycol reduction method to synthesize 2.6 nm Pt NPs *in situ* in the nanoporous wall of 766 nm carbonaceous flasklike nanoparticles (CFNPs) to construct ualtrasmall Pt NPs-modified flasklike colloidal motors (Pt-FCMs). The Pt NPs with an ultrasmall, uniform size and no ligand modification are supported by the carbonaceous flasklike nanoparticles. The Pt-FCMs are propelled by highly efficient catalytic decomposition of H_2O_2 fuels and exhibit ultrafast velocity. The instantaneous velocity observed at 5% H_2O_2 can reach up to about 134 μm s^{-1}, equivalent to 180 bodylength per second. The motion performance of Pt-FCMs is excellent for nanoscale and non-bubble propelled colloidal motors, surpassing that of the bubble-propelled flasklike colloidal motors at the same concentration of H_2O_2.[22,23] In addition to ultrafast mobility, Pt-FCMs display an enhanced ion tolerance, due to high catalytic activity of ultrasmall-sized Pt NPs in the carbonaceous wall. Furthermore, the direction of motion could be reversed by adding the cationic surfactant cetyltrimethylammonium bromide (CTAB). The self-propelled Pt-FCMs demonstrate a powerful, novel strategy towards ultrafast, highly ion-tolerant, and adaptable nanoscale colloidal motors by integrating highly active nanoparticles into the asymmetrical flasklike structures, which paves a promising way to realize the applications of chemically powered colloidal motors in complex media.

Experimental section

Materials and instruments

Sodium oleate (SO), poly(ethylene glycol)-*block*-poly (propylene glycol)-*block*-poly (ethylene glycol) (EO_{20}-PO_{70}-EO_{20}, P123), D-ribose, H_2PtCl_6, NaCl, sodium dodecyl sulfate (SDS), and cetyltrimethylammonium bromide (CTAB) were purchased from Sigma-Aldrich Co., Ltd. Ethylene glycol (EG), NaOH, hydrogen peroxide (H_2O_2), fetal bovine serum, and ethanol were purchased from Shanghai Aladdin Biochemical Technology Co., Ltd. Deionized water (Millipore) of 18.2 MΩ cm was used for all experiments. These commercial chemicals were directly used without further purification. The transmission electron microscope (TEM) images were obtained by Tecnai G2 F30 (FEI). The X-ray diffractometer (XRD) measurements were performed by using D8 ADVANCE (Bruker). The Zeta potential measurements were performed by a Malvern Zetasizer Nano-ZS. The movements were observed by Olympus CKX41 inverted optical microscope equipped with a 100× oil lens.

Synthesis of CFNPs

The CFNPs were synthesized according to the method described in the previous report.[24] First is the synthesis of polymeric flasklike nanoparticles (PFNPs). Briefly, 0.0555 g of SO and 0.0653 g of P123 were dissolved in 25 mL of deionized water, while 4.5 g of D-ribose was dissolved in 45 mL of deionized water. The D-ribose solution was then added to the mixture solution of SO and P123 and stirred at room temperature for 30 min before being transferred into a 100 mL autoclave. The reaction mixture was hydrothermally treated at 160 °C for 12 h. The synthesized PFNPs were harvested *via* centrifugation and washed with ethanol and deionized water three times respectively and then dried overnight. The CFNPs were obtained through temperature-programmed calcinating of PFNPs under the Ar atmosphere. Initially, the PFNPs underwent calcination at a rate of 10 °C min^{-1} until reaching 600 °C, and then remained at this temperature for 1 h before being further calcined to 900 °C at a rate of 5 °C min^{-1} for another hour.

Synthesis of Pt-FCMs

The Pt-FCMs were synthesized *via in situ* growth of Pt NPs on CFNPs using ethylene glycol reduction. Specifically, 50 mg of CFNPs were dispersed in a mixed solution of 50 mL of EG and 140 mL deionized water and then mixed with 10 mL of 20 mM H_2PtCl_6 solution under ultrasonic conditions for 30 min to promote the adsorption of the Pt precursor on the CFNPs. The pH of the mixture solution was adjusted to 12.5 by adding NaOH (1 M), followed by refluxing at 130 °C for 3 h to reduce the Pt precursor. Finally, Pt-FCMs were collected by centrifugation and washing.

Movement observation

The Pt-FCMs were mixed with the substrate solution, which can be the pure H_2O_2 solution with different concentrations or H_2O_2 solution containing NaCl or surfactant. The concentration of each component in the substrate was adjusted by adding volume. Subsequently, 10 μL of the mixture was dropped on the hydrophilic glass slide. The movement of Pt-FCMs was observed by using an Olympus CKX41 inverted optical microscope equipped with a 100× oil lens. The videos were captured by CCD camera at a frame rate of 40 fps and the length of the videos was 20 s.

Movement analysis

Motion coordinates were acquired using the Image J software. The mean squared displacement (MSD) of Pt-FCMs was calculated from motion coordinates according to the equation

$$\mathrm{MSD} = \left\langle \sum_{i}^{n} \left(r_i(t+\Delta t) - r_i(t)\right)^2 \right\rangle$$

where $r_i(t)$ are the coordinates of Pt-FCMs at time t. In this paper, all MSD curves are calculated by using the MATLAB code.[25] To improve the statistical robustness, 30 Pt-FCMs were counted and only the data in the initial 2 s were used to plot

the MSD curves. The self-propelled velocity (V_S) was obtained by fitting the data of the first 10 frames (Δt = 0.25 s, $\Delta t \ll \tau_R$) with equations MSD = $4D_0\Delta t + V_S^2\Delta t^2$, where τ_R is rotational time, D_0 is the diffusion coefficient of Brownian motion. Translational diffusion coefficient D was obtained by fitting the data of the last 20 frames (1.5 s–2 s, $\Delta t \gg \tau_R$) with the equation MSD = $4D\Delta t$ to MSD curve. The average velocity (V_A) is calculated as the total distance divided by the time, where the total distance is the sum of the distances between two adjacent frames.

Simulation of the concentration gradient field

The chemical concentration gradient field of reactant H_2O_2 and product O_2 (generated by Pt NPs on both the outside and inside surfaces catalyzed H_2O_2 decomposition) around the Pt-FCMs were simulated based on the Fick's law $F_i = -D_i\partial c_i$ (i = H_2O_2 or O_2) with F the species flux, D_i the diffusion coefficient, ∂c the chemical concentration gradient. Due to the D_i of H_2O_2 and O_2 in water being almost the same, the self-generated local concentration field around the Pt-FCMs is at the same magnitude with opposite direction in terms of the steady-state $\nabla^2 c_i = 0$ and non-convective diffusion approximation.

Results and discussion

Fig. 1A illustrates the preparation of Pt-FCMs. Firstly, PFNPs were synthesized *via* the soft-templating polymerization method, through the process of formation of nanoemulsion, the formation of opening, and the formation of necks. Subsequently, CFNPs which serve as the framework of the colloidal motor were obtained by calcining the PFNPs under the Ar atmosphere. Finally, the Pt NPs are synthesized *in situ* within the nanoporous wall of the CFNPs using the improving

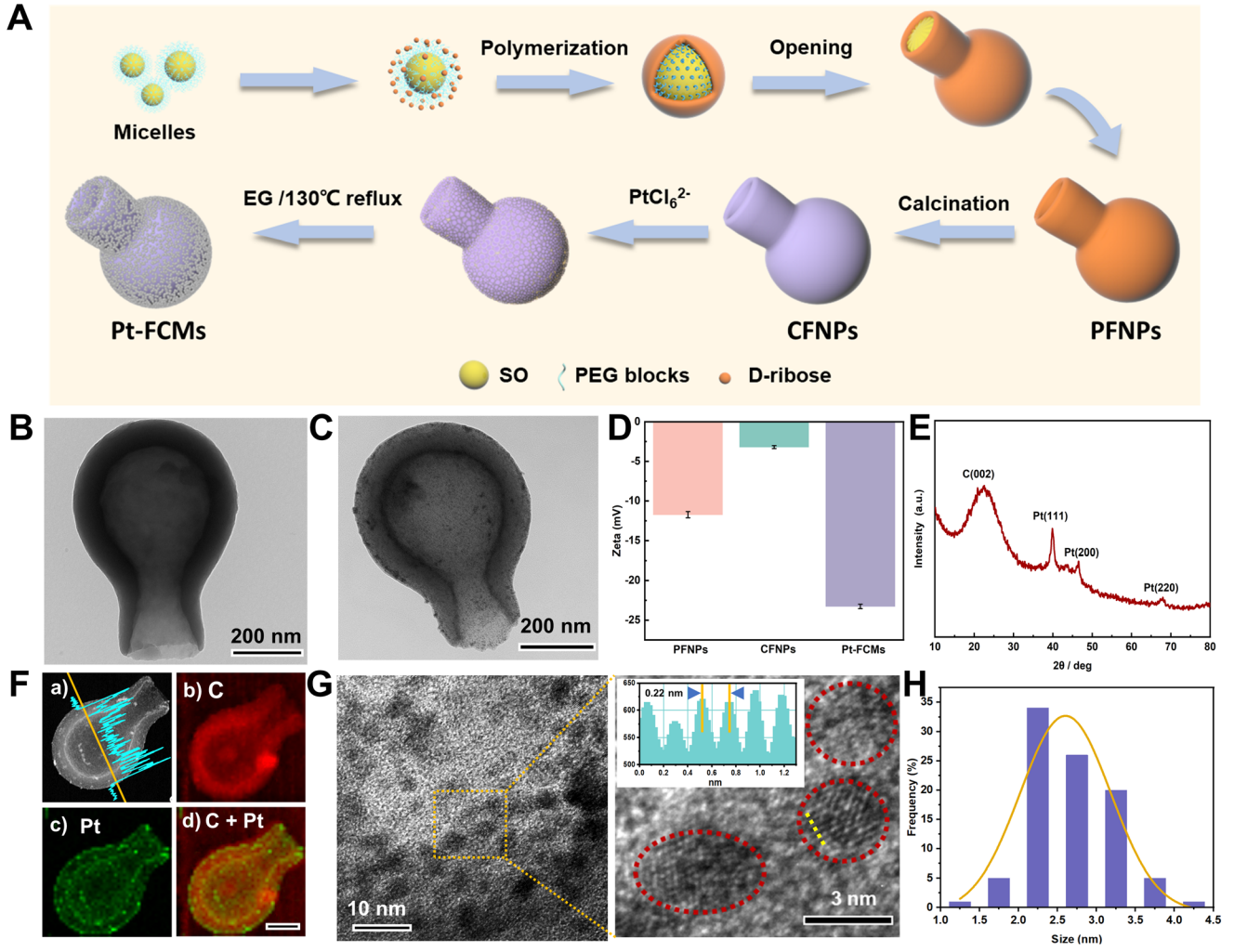

Fig. 1 Synthesis and characterization of Pt-FCMs. (A) Schematic diagram of the synthesis of the Pt-FCMs, which briefly includes the preparation of PFNPs by soft-templating polymerization, the preparation of CFNPs by carbonization of PFNPs, and *in situ* growth of Pt NPs on CFNPs. (B) TEM image of CFNPs. (C) TEM image of Pt-FCMs. (D) Zeta potential analysis of PFNPs, CFNPs, and Pt-FCMs. (E) XRD pattern of Pt-FCMs. (F) EDX elemental analysis: (a) STEM image of Pt-FCMs, the blue curve is the EDX line scan analysis of Pt element; (b–d) EDX mapping of the C, Pt, and the overlay of C and Pt. Scale bar is 200 nm. (G) HRTEM images of Pt-FCMs. (H) Size distribution of Pt NPs obtained from HRTEM images.

ethylene glycol reduction method. The CFNPs were characterized by TEM (Fig. 1B) and exhibit a typical flasklike morphology with a cavity that is connected to the outside. Their average bodylength is 766 ± 81 nm, the width of the spherical bottom is 439 ± 16 nm, and the wall thickness of the bottom of the CFNPs is about 96 ± 7 nm (N = 50). It has been proven that the wall of CFNP has abundant nanopores and high adsorption capacity.[26] The $PtCl_6^{2-}$ are adsorbed in the nanoporous wall and reduced by EG to form Pt NPs. Notably, no ligands are needed in the synthesis process. The successful modification and morphology of Pt NPs were confirmed using the TEM, zeta potential, XRD, scanning TEM (STEM), and energy-dispersive X-ray (EDX) analysis. The TEM image in Fig. 1C shows the flasklike shape of Pt-FCMs. In contrast to the smooth surface of CFNPs (Fig. 1B), numerous small black dots that are corresponding to Pt NPs are observed in the nanoporous wall. Fig. 1D shows the zeta potentials of PFNPs, CFNPs and Pt-FCMs with negative values. The Pt-FCMs exhibit a large potential difference with CFNPs, which may be attributed to the adsorption and reduction of $PtCl_6^{2-}$, resulting in a more negative potential. The XRD pattern of Pt-FCMs is shown in Fig. 1E, which exhibits diffraction peaks at 22.3°, 39.8°, 46.4°, and 67.9° are assigned to C (002), Pt (111), Pt (200), and Pt (220),[27] respectively, further confirming the presence of Pt. Moreover, the high-angle annular dark-field (HAADF) STEM image coupled with EDX element analyses in Fig. 1F are used to characterize the modification of the Pt NPs in the nanoporous wall. These results show that the Pt NPs are uniformly dispersed in nanoporous wall, except a few regions which implying the aggregates of Pt NPs. The bright blue curve in Fig. 1F (a) represents the EDX line scanning for the Pt element content at the yellow line position. A high Pt content is observed on both inner and outer walls of Pt-FCMs, suggesting the distribution of Pt NPs on both inner and outer surfaces of CFNPs. The high-resolution TEM (HRTEM) images presented in Fig. 1G reveal that most of Pt NPs are isolated. The inset of Fig. 1G shows the interplanar crystal spacing of Pt NPs is 0.22 nm, which can be ascribed to Pt (111). The size distribution of Pt NPs was determined through measuring the diameters of 153 Pt NPs from multiple HRTEM images. The result as shown in Fig. 1H reveals a narrow size distribution of Pt NPs with an average diameter of 2.6 ± 0.11 nm. The ultrasmall and monodisperse Pt NPs without additional chemical modifications provide a high catalytic capacity for Pt-FCMs.

The autonomous motion of Pt-FCMs propelled by catalytic decomposition of H_2O_2 was investigated and two predominant motion modes of Pt-FCMs were observed as shown in Fig. 2A. In the absence of H_2O_2, the Pt-FCMs exhibit typical Brownian motion, while in the presence of H_2O_2, the Pt-FCMs display strong self-propelled motion. The time-lapse images in Fig. 2B and C and the corresponding videos (Video S1 and Video S2†) show the quasi-linear trajectory and the quasi-circular trajectory of Pt-FCMs in 5% H_2O_2, respectively. As can be seen, the Pt-FCMs moved from the flask bottom to the opening and no bubbles were observed to form on their surface, indicating that the colloidal motors are propelled by the self-phoretic effect induced by chemical reaction on both inner and outer surfaces. Within 3 s, the Pt-FCMs with both motion modes travel a considerable distance. The Pt-FCMs showing a quasi-circular motion trajectory in Fig. 2C completed 12 circles of motion. The quasi-circular motion behaviour can be attributed to the distribution difference of Pt NPs on the Pt-FCMs.

To further investigate the motility of Pt-FCMs, we examined the autonomous motion of the Pt-FCMs in H_2O_2 solutions with different concentrations. Among the two motion modes of Pt-FCMs, the quasi-circular trajectories cannot produce effective motion displacement despite having a high average velocity (V_A). Therefore, the statistics of motion trajectories, MSD, and self-propelled velocity (V_S) fitted from MSD in Fig. 3 only involve Pt-FCMs with the quasi-linear trajectories. The statistics of V_A include all sorts of motion trajectories. Fig. 3A displays the trajectories within 3 s at different concentrations of H_2O_2. As the concentration of H_2O_2 increases, so does the effective displacements of Pt-FCMs, indicating the improved directional motion of the colloidal motors. Fig. 3B depicts the MSD analysis used to quantify the autonomous motion. In the absence of H_2O_2, the MSD follows a typical linear curve that represents Brownian motion. With an increasing concentration of H_2O_2, MSD exhibits a typical parabolic curve indicative of autonomous motion. The slope also gradually increases, indicating the enhancement of the autonomous motion. Fig. 3C shows the translational diffusion coefficient (D) of the Pt-FCMs. The diffusion coefficient of Brownian is approximately 0.33 $\mu m^2\ s^{-1}$. At a concentration of 0.01% H_2O_2, there is a slight increase in D. At the concentration of 0.1% H_2O_2, the D value increases significantly and reaches about 3 times that of Brownian motion. Particularly, when the concentration of H_2O_2 rises to 5%, the D reaches approximately 4.99 $\mu m^2\ s^{-1}$, a diffusion ability 15 times greater than that observed with Brownian motion. Fig. 3D depicts the V_S of Pt-FCMs at the various concentrations of H_2O_2. The V_S gradually increases with the increasing H_2O_2 concentration, reaching *ca.* 9 $\mu m\ s^{-1}$ at 5% H_2O_2. These results demonstrate that the Pt-FCMs with quasi-linear motion mode exhibit excellent directional motility. As shown in Fig. 3E, the V_A accelerates with an increase in H_2O_2 concentration. The V_A of Pt-FCMs increased from 4.49 $\mu m\ s^{-1}$ at 0.01% H_2O_2 to 23.32 $\mu m\ s^{-1}$ at 5% H_2O_2. The inset in Fig. 3E illustrates the distribution of V_A for colloidal motors in 5% H_2O_2, revealing that most Pt-FCMs exhibit average velocities within a range of 10–20 $\mu m\ s^{-1}$, followed by 20–30 $\mu m\ s^{-1}$ and 30–40 $\mu m\ s^{-1}$. It is worth noting that the V_A of the Pt-FCMs in 5% H_2O_2 exhibits significant variation, which may be attributed to individual differences among colloidal motors during the synthesis process. Fig. 3F displays the instantaneous velocities of a typical colloidal motor with ultrafast mobility in quasi-circular mode (corresponding trajectory in Fig. 2C). The fastest velocity of 134 $\mu m\ s^{-1}$ was observed, which is equivalent to 180 bodylength per second. These results, especially V_S and V_A, indicate that the Pt-FCMs possess strong motion activity. It is worth noting that no bubble nucleation and rupture was observed on the surface of the Pt-FCMs in this study. We conducted a comparative analysis of

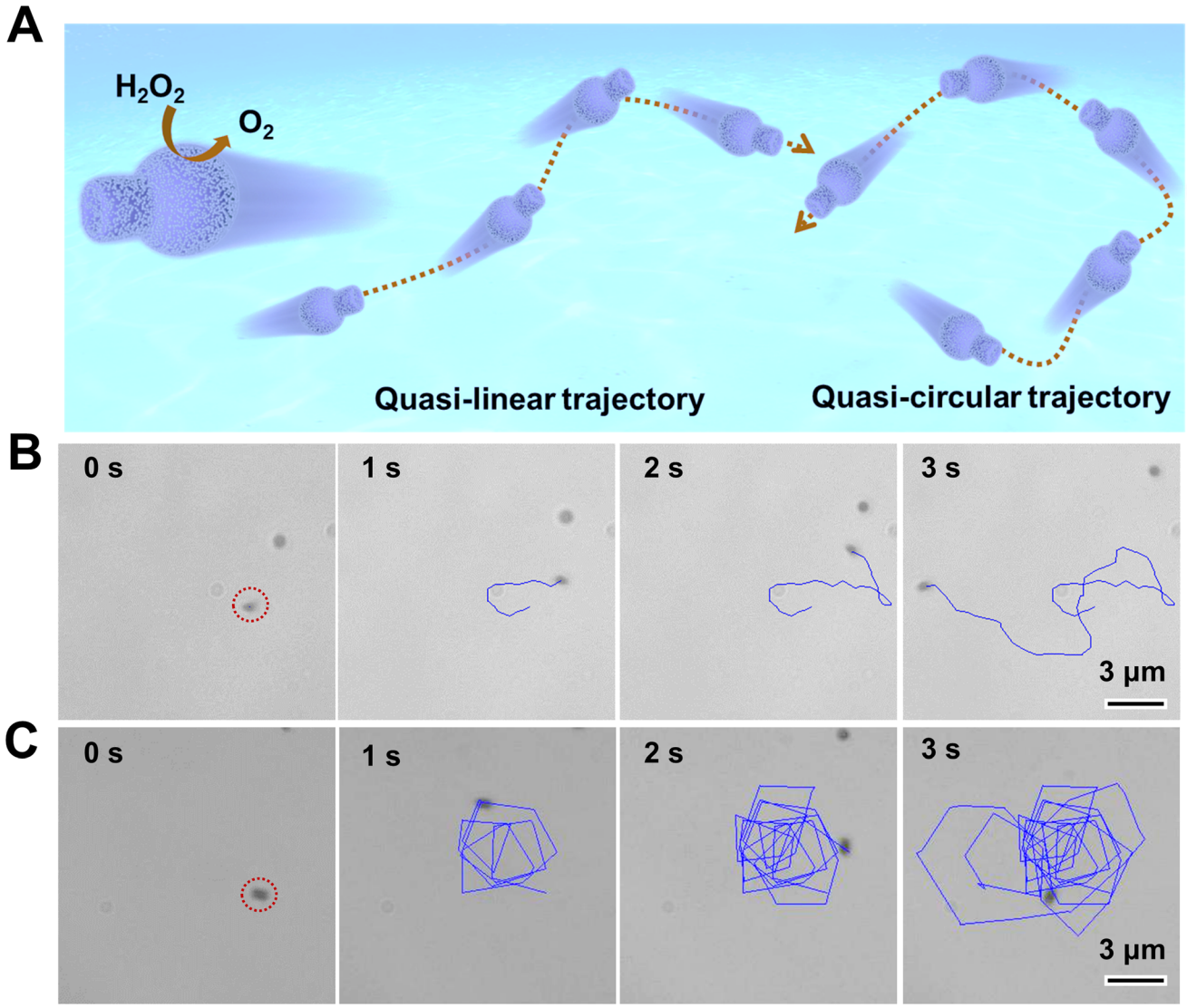

Fig. 2 Motion behaviour of Pt-FCMs in H_2O_2 solutions. (A) Schematic diagram of Pt-FCMs propelled by the catalytic decomposition of H_2O_2 and their quasi-linear trajectories and quasi-circular trajectories. (B) Time-lapse images of quasi-linear motion of Pt-FCMs within 3 s at 5% H_2O_2. (C) Time-lapse images of quasi-circular motion of Pt-FCMs within 3 s at 5% H_2O_2.

the motion performance between Pt-FCMs and other chemically powered colloidal motors with similar shapes, including flask,[22,23,28–30] tadpole[31] and stomatocyte[32–34] types. As shown in Table S1,† Pt-FCMs exhibit superior motion performance compared with colloidal motors propelled by self-phoretic effort,[23,28] and even outperform certain bubble-propelled colloidal motors at a concentration of 5% H_2O_2.[22,23] As mentioned later, propulsion based on the release of nanobubbles should be excluded from contributing to the motion velocity of Pt-FCMs. The high mobility of Pt-FCMs challengs a widely accepted opinion that bubble-propulsion provides colloidal motors with faster velocity than self-phoretic propulsion. Several similarly shaped (not so similar) and smaller sized colloidal motors such as stomatocyte-shaped nanomotors do have greater velocities than that of Pt-FCMs.[32–34] However, Pt-FCMs represent a new type of colloidal motors with high mobility. The exceptional velocity of Pt-FCMs could be attributed to the well-dispersed ultrasmall and ligand-free Pt nanoparticles within the nanoporous carbonaceous wall, which exposes a greater number of active sites and results in heightened catalytic ability.

In addition to the ultrafast velocity, the influence of ionic strength on the motility of Pt-FCMs was also tested. The motion behaviour of Pt-FCMs was observed in 5% H_2O_2 with different concentrations of NaCl. Fig. 4A illustrates the trajectories of Pt-FCMs with a duration of 3 s at 5% H_2O_2 at different concentrations of NaCl. The displacements of Pt-FCMs exhibit a negative correlation with increasing NaCl concentrations. Fig. 4B displays the MSD curves. At a NaCl concentration of 0.5 mM, the MSD is a typical parabolic curve. With increasing NaCl concentration to 5 mM, the slope of MSD curve decreases despite the curve still being a parabolic one.

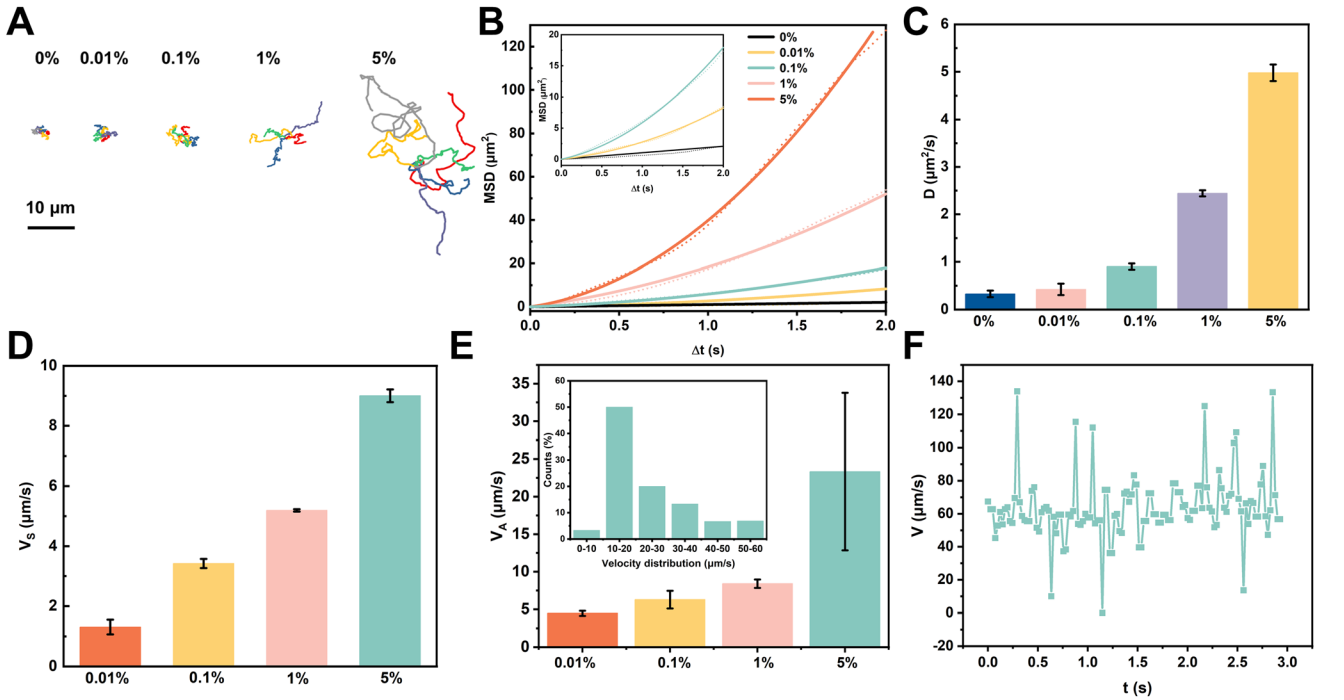

Fig. 3 Motion analysis of Pt-FCMs. (A) Motion trajectories of Pt-FCMs at 0%, 0.01%, 0.1%, 1%, and 5% H_2O_2 within 3 s. (B) Mean square displacement (MSD) curves of Pt-FCMs at H_2O_2 concentrations of 0%, 0.01%, 0.1%, 1%, and 5%, and (C) the corresponding translational diffusion coefficients (D) obtained from MSD curves. (D) Self-propelled velocity (V_S) of Pt-FCMs at 0.01%, 0.1%, 1%, and 5% H_2O_2 obtained from MSD. (E) Average velocity (V_A) of Pt-FCMs at 0.01%, 0.1%, 1%, and 5% H_2O_2. The inset is the average velocity distribution of Pt-FCMs in 5% H_2O_2. (F) The instantaneous velocity of Pt-FCMs in quasi-circular motion mode at 5% H_2O_2. The scale bar is 5 μm.

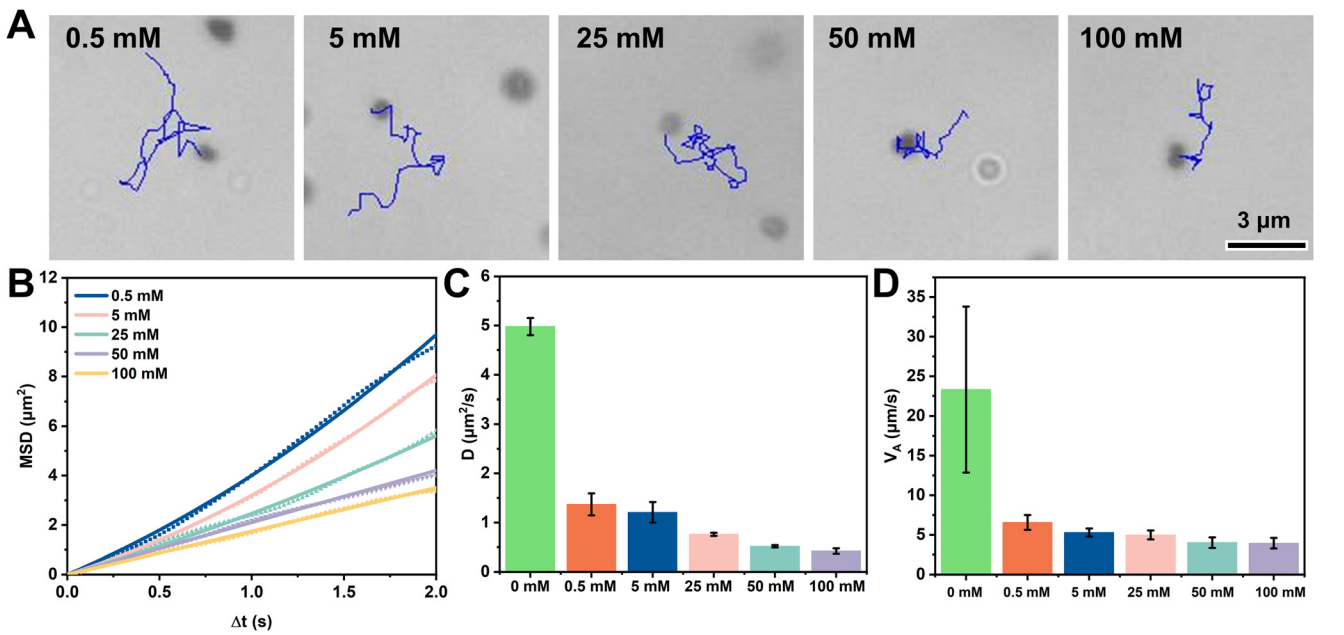

Fig. 4 Ion tolerance of Pt-FCMs. (A) Motion trajectories of Pt-FCMs at 5% H_2O_2 in the presence of 0.5 mM, 5 mM, 25 mM, 50 Mm, and 100 mM NaCl within 3 s. (B) MSD curves of Pt-FCMs at 5% H_2O_2 in the presence of NaCl. The (C) Diffusion coefficients (D) at 5% H_2O_2 in the presence of NaCl. (D) Average velocity (V_A) of Pt-FCMs at 5% H_2O_2 in the presence of NaCl.

When 25 mM of NaCl solution is applied, the MSD curve becomes to be linear. When the NaCl concentration increases to 50 mM and 100 mM, the MSD curves are linear with a decreasing slope even though the slopes are larger than that of Brownian motion. This result suggests that the directionality of the motion of the Pt-FCMs has been weakened with the enhanced rotational motion when increasing the ionic strength. Fig. 4C and D show the D and V_A of the Pt-FCMs in the presence of different concentrations of NaCl, respectively. The EI_{50} of Pt-FCMs in 5% H_2O_2 is less than 0.5 mM, where EI_{50} represents the ionic concentration at which the colloidal motors can move at 50% speed of that without electrolytes.[15] With the increase of NaCl concentration, the D and V_A decrease slowly. When the NaCl concentration is 100 mM, the D remains 1.68 times larger than that of Brownian motion. This result indicates that the ionic strength exerts a significant impact on the motion activity, but not fatal enough. Although their ion tolerance performance is not so good at lower ionic strength, Pt-FCMs still exhibit a certain degree of mobility at 100 mM NaCl and a diffusion coefficient that exceeds Brownian motion by a factor of 2 at 25 mM NaCl and by a factor of 4.7 at 5 mM NaCl. Compared to the fatal effect of 1 mM NaCl on the movement of microscale Pt-polystyrene motors,[14] the performance of ion tolerance of Pt-FCMs is relatively improved. The motility of Pt-FCMs in complex fluids was further verified, as evidenced by efficient movement (Video S3†) observed in 50% fetal bovine serum containing 5% H_2O_2. Notably, the V_A is 4.12 μm s^{-1}, and the D of Pt-FCMs remains at 0.85 μm^2 s^{-1}, which is 2.5 times faster than Brownian motion. There are several possible reasons for the enhanced ion tolerance. One of the reasons is the nanoscale size of Pt-FCMs. It has been reported that decreasing the size of colloidal motors into the nanometer scales can improve ion tolerance.[3] Secondly, Pt-FCMs may produce nanobubbles that are invisible in the present microscopic observation. However, the experimental results show that adding the NaCl solution can significantly affect the motion velocity of Pt-FCMs, which is inconsistent with the phenomenon that the ionic strength has little effect on the mobility of bubble-propelled colloidal motors.[35] Therefore, bubble propulsion should have little contribution to the motion and ion tolerance of Pt-FCMs. Finally, it is highly probable that the ion tolerance primarily stems from the high catalytic activity of the ultrasmall ligand-free Pt NPs on the carbonaceous surface and the flask-shaped structure of Pt-FCMs, which compensates for the adverse effects of ionic strength on the motor motion.

When ionic surfactants are added to the fuel solution, it is found that Pt-FCMs exhibit interesting motion behaviours. Fig. 5A and B show the trajectories of Pt-FCMs in 3 s in the presence of 0.9 mM CTAB and 8 mM SDS at 5% H_2O_2, respectively. Fig. 5C shows the V_A of Pt-FCMs when adding different surfactants. These results indicate that the V_A of Pt-FCMs

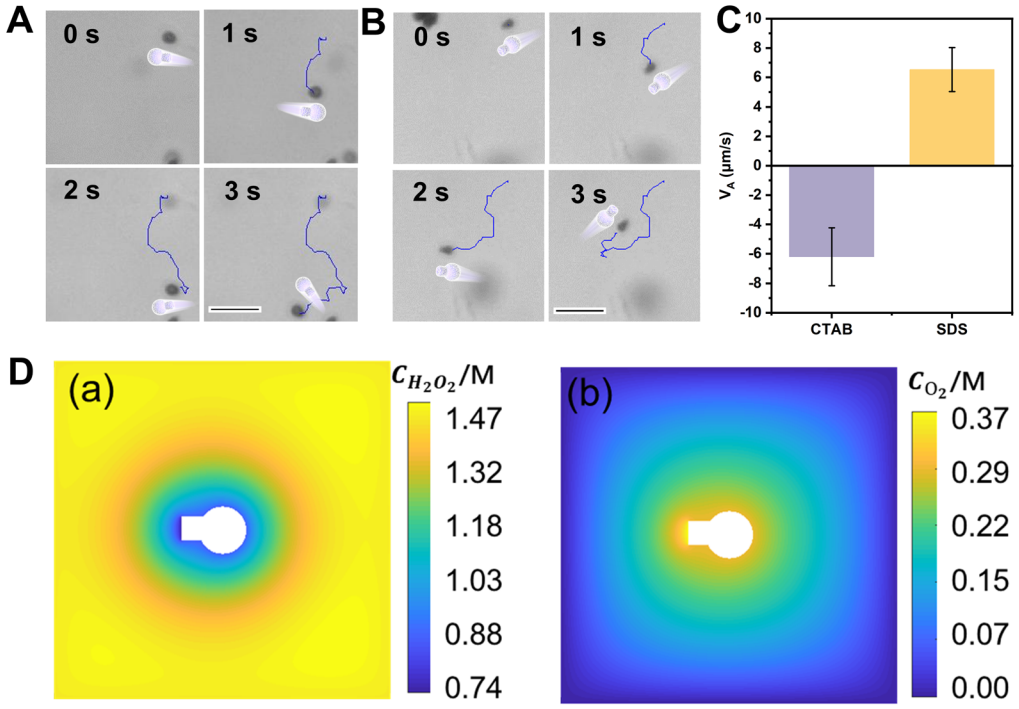

Fig. 5 Motion behaviour of Pt-FCMs in the presence of ionic surfactants. (A) Time-lapse images of locomotive Pt-FCMs in the presence of CTAB, the motion direction is the opening backward. Scale bar is 3 μm. (B) Time-lapse images of locomotive Pt-FCMs in the presence of SDS, the motion direction is the opening forward. Scale bar is 3 μm. (C) The average velocity (V_A) of Pt-FCMs in the presence of ionic surfactant. (D) Simulated chemical concentration gradients of (a) reactant H_2O_2 and (b) product O_2, generated by the catalyzed reaction occurring on both the outside and inside surface of Pt-FCMs.

decreases in both surfactant solutions due to the increase of ionic strength caused by the addition of ionic surfactants. Interestingly, the motion direction of Pt-FCMs was reversed in the presence of cationic surfactant CTAB. As shown in Fig. 5A and Video S3,† Pt-FCMs move with the orientation from the flask opening to the flask bottom (the corresponding velocity is defined as a negative value). Conversely, in the presence of SDS, the motion direction of Pt-FCMs is still oriented from the bottom to the opening (Fig. 5B and Video S4†). Previous studies have demonstrated that the change in the surface wettability of the colloidal motors can reverse the motion direction.[28] The reason for the reversal of the direction of the Pt-FCMs in the presence of CTAB may be that the positively charged hydrophilic group of CTAB adsorbs with the negatively charged Pt-FCMs due to electrostatic interaction. The hydrophobic group of CTAB is outward, which makes the surface of the motor more hydrophobic. For the anionic surfactant SDS, the hydrophobic group is preferentially adsorbed onto the surface of the negatively charged colloidal motors compared to its negatively charged hydrophilic group. The outward-facing hydrophilic group does not induce a remarkable change in surface wettability and thus the motion direction remains unaffected in the presence of SDS. The Pt-FCMs propelled by the catalytic decomposition of H_2O_2 generate O_2 and H_2O_2 concentration gradients, as depicted by the simulation results in Fig. 5D. These concentration gradients have the same order of magnitude but are opposite in directions. When the surface wettability of the Pt-FCMs changes, the interaction between O_2 and H_2O_2 molecules and the surface of the colloidal motor is affected, which results in the change of the concentration gradient field that plays a dominant role in determining the direction of motion, and finally leads to the direction reversal.

Conclusions

In conclusion, we employed the ethylene glycol reduction method to synthesize well-dispersed Pt NPs with the ultrasmall and uniform diameter of 2.6 nm in the nanoporous wall of carbonaceous flasklike nanoparticles for constructing the chemically powered Pt-FCMs. The Pt-FCMs achieve ultrafast velocity propelled by the self-phoretic effect. At 5% H_2O_2, the velocity can reach up to about 134 μm s^{-1} (180 bodylength per s). The motion activity of Pt-FCMs even exceeds that of bubble-propelled flasklike colloidal motors, challenging the previous cognition that bubble-propulsion has high motion activity. In addition to exhibiting high mobility, Pt-FCMs also show enhanced ion tolerance even when adding 100 mM NaCl, and an adaptive direction reversal in the presence of CTAB. As demonstrated by Pt-FCMs, compared with the methods such as the sputter coating of metal and the loading of ligand-modified nanocatalysts, the strategy of integrating ultrasmall ligand-free nanocatalysts with a high density of catalytically active sites could pave a promising way to access ultrafast, highly ion-tolerant, and adaptable colloidal motors for the applications in various complex scenarios.

Author contributions

Shurui Yuan: data curation, formal analysis, investigation, validation, writing-original draft. Ling Yang: formal analysis, methodology, resources, writing-review & editing. Xiankun Lin: conceptualization, data curation, funding acquisition, project administration, supervision, writing-review & editing. Qiang He: conceptualization, data curation, funding acquisition, project administration, supervision, writing-review & editing.

Conflicts of interest

There are no conflicts to declare.

Acknowledgements

This work was supported by the National Natural Science Foundation of China (22193033, U22A20346), Heilongjiang Provincial Natural Science Foundation of China (YQ2020B001) and Start-up Grant of Wenzhou Institute, University of Chinese Academy of Sciences (WIUCASQD2021044 and WIUCASQD2022029).

References

1 K. K. Dey and A. Sen, *J. Am. Chem. Soc.*, 2017, **139**, 7666–7676.
2 F. Z. Mou, X. F. Li, Q. Xie, J. H. Zhang, K. Xiong, L. L. Xu and J. G. Guan, *ACS Nano*, 2020, **14**, 406–414.
3 C. J. Wu, J. Dai, X. F. Li, L. Gao, J. Z. Wang, J. Liu, J. Zheng, X. J. Zhan, J. W. Chen, X. Cheng, M. C. Yang and J. Y. Tang, *Nat. Nanotechnol.*, 2021, **16**, 288–295.
4 Z. L. Liu, L. M. Gan, L. Hong, W. X. Chen and J. Y. Lee, *J. Power Sources*, 2005, **139**, 73–78.
5 W. Duan, R. Liu and A. Sen, *J. Am. Chem. Soc.*, 2013, **135**, 1280–1283.
6 A. A. Solovev, S. Sanchez and O. G. Schmidt, *Nanoscale*, 2013, **5**, 1284–1293.
7 C. Kaspar, B. J. Ravoo, W. G. V. D. Wiel, S. V. Wegner and W. H. P. Pernice, *Nature*, 2021, **594**, 345–355.
8 P. Fischer, *Adv. Mater.*, 2020, **32**, 1905953.
9 S. R. Yuan, X. K. Lin and Q. He, *J. Colloid Interface Sci.*, 2022, **612**, 43–56.
10 J. X. Li, B. Esteban-Fernández de Ávila, W. Gao, L. F. Zhang and J. Wang, *Sci. Robot.*, 2017, **2**, eaam6431.
11 M. Luo, Y. Z. Feng, T. W. Wang and J. G. Guan, *Adv. Funct. Mater.*, 2018, **28**, 1706100.
12 M. Safdar, S. U. Khan and J. Jänis, *Adv. Mater.*, 2018, **30**, 1703660.
13 X. Arqué, R. Mestre, B. Ciraulo, J. Ortega Arroyo, R. Quidant, T. Patiño and S. Sánchez, *Research*, 2020, **2020**, DOI: **10.34133/2020/2424972**.
14 A. Brown and W. Poon, *Soft Matter*, 2014, **10**, 4016–4027.

15 X. J. Zhan, J. Z. Wang, Z. Xiong, X. Zhang, Y. Zhou, J. Zheng, J. Chen, S.-P. Feng and J. Tang, *Nat. Commun.*, 2019, **10**, 3921.
16 V. Sridhar, F. Podjaski, Y. Alapan, J. Kröger, L. Grunenberg, V. Kishore, B. V. Lotsch and M. Sitti, *Sci. Robot.*, 2022, **7**, eabm1421.
17 Z. L. Yang, L. M. Wang, Z. X. Gao, X. M. Hao, M. Luo, Z. Yu and J. G. Guan, *ACS Nano*, 2023, **17**, 6023–6035.
18 T. S. Ahmadi, Z. L. Wang, T. C. Green, A. Henglein and M. A. El-Sayed, *Science*, 1996, **272**, 1924–1925.
19 W. X. Chen, J. Y. Lee and Z. L. Liu, *Chem. Commun.*, 2002, **21**, 2588–2589.
20 S. Y. Wang and X. Wang, *Nanotechnology*, 2008, **19**, 265601.
21 S. Y. Wang, S. P. Jiang, T. J. White, J. Guo and X. Wang, *J. Phys. Chem. C*, 2009, **113**, 18935–18945.
22 C. Zhou, C. Y. Gao, Z. H. Lin, D. L. Wang, Y. Li, Y. Yuan, B. H. Zhu and Q. He, *Langmuir*, 2020, **36**, 7039–7045.
23 T. Y. Liu, L. Xie, J. Zeng, M. Yan, B. L. Qiu, X. Y. Wang, S. Zhou, X. Zhang, H. Zeng, Q. R. Liang, Y. J. He, K. Liang, J. Liu, E. Velliou, L. Jiang and B. Kong, *ACS Appl. Mater. Interfaces*, 2022, **14**, 15517–15528.
24 C. H. Chen, H. Y. Wang, C. L. Han, J. Deng, J. Wang, M. M. Li, M. H. Tang, H. Y. Jin and Y. Wang, *J. Am. Chem. Soc.*, 2017, **139**, 2657–2663.
25 N. Tarantino, J.-Y. Tinevez, E. F. Crowell, B. Boisson, R. Henriques, M. Mhlanga, F. Agou, A. Israël and E. Laplantine, *J. Cell Biol.*, 2014, **204**, 231–245.
26 Y. J. Li, Q. Shi, Y. Luo, G. W. Chu, H. K. Zou, L. L. Zhang and B. C. Sun, *Chem. Eng. Sci.*, 2020, **225**, 115787.
27 P. S. Fernández, D. S. Ferreira, C. A. Martins, H. E. Troiani, G. A. Camara and M. E. Martins, *Electrochim. Acta*, 2013, **98**, 25–31.
28 C. Y. Gao, C. Zhou, Z. H. Lin, M. C. Yang and Q. He, *ACS Nano*, 2019, **13**, 12758–12766.
29 Y. C. Long, Q. H. Wu, X. Y. Zuo, G. L. Zhang, Z. X. Zhang, Z. Z. Yang and F. X. Liang, *ACS Nano*, 2022, **16**, 16690–16698.
30 D. L. Yi, Q. Zhang, Y. H. Liu, J. Y. Song, Y. Tang, F. Caruso and Y. J. Wang, *Angew. Chem., Int. Ed.*, 2016, **55**, 14733–14737.
31 M. Yan, L. Xie, B. L. Qiu, S. Zhou, T. Y. Liu, J. Zeng, Q. R. Liang, J. Y. Tang, K. Liang and D. Y. Zhao, *ACS Nano*, 2021, **15**, 11451–11460.
32 D. A. Wilson, R. J. Nolte and J. C. M. van Hest, *Nat. Chem.*, 2012, **4**, 268–274.
33 Y. Tu, F. Peng, X. Sui, Y. Men, P. B. White, J. C. M. van Hest and D. A. Wilson, *Nat. Chem.*, 2016, **9**, 480–486.
34 I. A. Pijpers, S. Cao, A. Llopis-Lorente, J. Zhu, S. Song, R. R. Joosten, F. Meng, H. Friedrich, D. S. Williams and S. Sánchez, *Nano Lett.*, 2020, **20**, 4472–4480.
35 W. Gao, S. Sattayasamitsathit, J. Orozco and J. Wang, *J. Am. Chem. Soc.*, 2011, **133**, 11862–11864.